ACADÉMIE
DES SCIENCES
INSTITUT DE FRANCE

Comptes Rendus
Mécanique

Ahmed Zouari, Samuel Forest, Sylvain Dépinoy, Yazid Madi, Jean-Michel Mataigne, Houssem Eddine Chaïeb, Pascal Bertho, Aymen Bouzid, Aurelien Chopin and Coralie Jung

Influence of steel substrate behavior on the deformation and cracking of Zn–Al–Mg coatings on galvanized steel sheets

Volume 353 (2025), p. 1425-1449

Online since: 15 December 2025

https://doi.org/10.5802/crmeca.340

The Comptes Rendus. Mécanique *are a member of the Mersenne Center for open scientific publishing*
www.centre-mersenne.org — e-ISSN : 1873-7234

ACADÉMIE DES SCIENCES
INSTITUT DE FRANCE

Comptes Rendus. Mécanique
2025, Vol. 353, p. 1425-1449
https://doi.org/10.5802/crmeca.340

Research article

Influence of steel substrate behavior on the deformation and cracking of Zn–Al–Mg coatings on galvanized steel sheets

Ahmed Zouari [*,a,b,c], **Samuel Forest** [*,a], **Sylvain Dépinoy** [a], **Yazid Madi** [a], **Jean-Michel Mataigne** [b], **Houssem Eddine Chaïeb** [d], **Pascal Bertho** [b], **Aymen Bouzid** [b], **Aurelien Chopin** [b] **and Coralie Jung** [b]

[a] Mines Paris PSL University, Centre des matériaux, CNRS UMR 7633, 21 Allée des Marronniers, 78000 Versailles, France

[b] ArcelorMittal Maizières Research, voie Romaine, F-57280, Maizières les Metz, France

[c] Safran Aircraft Engines Villaroche, Rond-Point Rene Ravaud, 77550 Moissy-Cramayel, France

[d] ArcelorMittal Global R&D Ghent, J.F. Kennedylaan 3, B-9060 Zelzate, Belgium

Current address: Safran Aircraft Engines Villaroche, Rond-Point Rene Ravaud, 77550 Moissy-Cramayel, France (A. Zouari)

E-mails: Ahmed.Zouari@safrangroup.com (A. Zouari), Samuel.Forest@minesparis.psl.eu (S. Forest)

Abstract. The objective of this study is twofold: (i) to comprehensively describe the deformation modes of zinc coatings depending on their crystallographic texture and (ii) to investigate the effect of Lüders banding occurring in the steel substrate on the coating deformation and cracking modes. Microscopic characterization and mechanical tests were conducted on three types of galvanized steel: a mild steel substrate and a high-strength low-alloy (HSLA) steel substrate known to exhibit the Lüders banding phenomenon, and a dual-phase steel substrate. The results reveal a direct correlation between the coating texture, plastic deformation modes, and the mechanical behavior of the respective substrates. Digital Image Correlation (DIC) was employed to measure the strain fields and characterize strain localization phenomena resulting from Lüders banding. The strain field measured on the galvanized substrate specimens showed that Lüders band propagation leads to accelerated plastic deformation and cracking in the Zn–Al–Mg coating. Finite element simulations were performed by considering the real coating microstructure and incorporating the macroscopic behavior of the substrate. The simulation results demonstrate that slip and twinning activities of the coating grains are strongly influenced by the underlying substrate behavior.

Keywords. Zinc coatings, Crystallographic texture, Lüders banding, Coating cracking, Slip and twinning, Strain localization, Galvanized steel.

Manuscript received 1 June 2025, revised 19 October 2025, accepted 4 November 2025.

* Corresponding authors

1. Introduction

In recent years, significant efforts have been made to enhance the properties of zinc coatings by introducing new chemical elements into the zinc bath during the hot-dip galvanizing (HDG) process [1]. These elements aim at improving corrosion resistance by adding Al and Mg to zinc [2–4]. However, the incorporation of these elements leads to substantial changes in the microstructure and crystallographic texture of the coatings, which in turn directly impacts their mechanical behavior and adhesion performance during forming and shaping processes.

Previous research has primarily focused on investigating the impact of microstructure and crystallographic orientation on the deformation and cracking behaviors of Zn grains [5–12]. These studies have revealed that the morphology of zinc grains and of eutectic phases can be considerably affected by the relatively low variations of Al and Mg [13]. Furthermore, inclusion of Mg in zinc coatings induces the formation of a brittle binary eutectic phase (i.e. Zn + $MgZn_2$) which acts as the primary cause of micro-cracking within Zn–Al–Mg coatings [14].

Plastic slip activity of Zinc alloy coatings has been investigated by Parisot et al. [15] in two different coating microstructures and also in bulk zinc using uniaxial tension, plane-strain tension, and expansion loading. This study demonstrates that the primary deformation mechanism is basal slip in bulk zinc and in the recrystallized coatings. However, in temper rolled coatings or "Skin Pass" coatings, and in non-temper rolling, the major modes of deformation are identified as pyramidal π^2 slip and mechanical twinning, which are additional characteristic deformation modes in hcp metals and alloys. A specific study regarding the deformation of Zn–Al–Mg coatings was conducted by Ahmadi et al. [13] using an in-situ uniaxial tensile test followed by Electron-Back-Scattered Diffraction (EBSD) analyses and SEM observations. These authors showed that zinc grains can develop five independent slip/twinning systems, namely basal, prismatic, 2nd order pyramidal, 1st order pyramidal and twinning.

Park et al. [8] examined the effect of the crystallographic orientation of Zn grains on the cracking of two Zn–Al–Mg coatings by combining mechanical deformation and post-mortem EBSD analyses. They demonstrated that the primary zinc and eutectic zinc phases, characterized by basal planes with the [0001] direction perpendicular to the normal direction (ND) of the sheet, are particularly prone to cracking when subjected to stress along the *c*-axis. Jaffrey et al. [16] presented experimental evidence that non-basal grains exhibited a greater occurrence of cleavage cracks compared to other oriented grains. According to Parisot et al. [17], the occurrence of cleavage cracking in the coatings is influenced by the favored orientations of the grains. They observed that the maximum normal stress component required for cleavage to take place is highest in grains that have their *c*-axis aligned along the tensile direction.

The existing research exploring the impact of the steel substrate on the deformation and cracking behavior of Zn–Al–Mg alloy coating is notably limited. A particular gap exists in understanding the strain localization behavior of zinc grains, in the presence of Lüders banding of the steel substrate. Only two notable studies, conducted by Parisot et al. and Ahmadi et al., have explored this aspect [13,17]. Parisot et al. focused on Zn–Al coating on interstitial-free steel, while Ahmadi et al. investigated the effect of HSLA steel with Lüders banding and IF steel on Zn–Al–Mg coating cracking behavior. However, a comprehensive understanding of the underlying substrate influence on coating deformation and cracking has not been thoroughly scrutinized or clarified. How does the Lüders band arising from the substrate propagate into the coating? Moreover, there is a need for a better understanding of the impact of Lüders band propagation on coating formability, taking into account real microstructural factors. This crucial aspect has never been thoroughly investigated through simulations that incorporate the actual microstructure, allowing for a detailed examination of how Lüders band influences the deformation behavior of the coating.

Therefore, it is crucial to better understand the interplay between the coating, including its microstructure and crystallographic texture, and the substrate through appropriate experimental and numerical investigations. To address this research gap, the present study aims at gaining a comprehensive understanding of the effect of steel substrate on the formability of zinc coatings. This investigation takes into account various factors such as the microstructure of the coating, the crystallographic orientation of the phases and the influence exerted by the underlying steel substrate. In pursuit of this objective, we have examined three specific types of steel substrates with different hardening behavior, namely Mild, HSLA, and Dual-Phase steels. These substrates were coated with an identical Zn–Al–Mg alloy. The materials were tested in tension and some tests were interrupted to follow the propagation of the Lüders band through the coating and identify the deformation and cracking modes. A three-dimensional finite-element crystal-plasticity simulation of a zinc coating on a galvanized steel sheet has been performed to assess the local impact of substrate behavior and give access to mechanical and physical quantities that are experimentally challenging to measure. These quantities include the effect of Lüders banding on the coating local strain field, the slip activities in each grain as well as the strain gradient throughout the coating thickness. The simulation takes into consideration the actual polycrystalline structure of the coating, providing valuable insights into the material behavior that would otherwise be difficult to obtain experimentally.

The microstructures and textures of the samples are described in Section 2. Uniaxial and equi-biaxial mechanical tests coupled with digital image correlation techniques to characterize strain localization due to Lüders banding for the coated mild steel (C_Mild) and the coated HSLA steel have been conducted and are presented in Section 3. In the same section, the results of the mechanical tests are presented. The effect of the crystallographic orientation and microstructure of Zn grains on plastic deformation modes such as plastic slip, deformation twinning and cracking modes have been investigated by combining mechanical deformation, post-mortem Scanning Electron Microscopy (SEM) observations and EBSD analyses. Section 4 of the study introduces the numerical method employed to model the propagation of Lüders banding within the substrate and the coating and to simulate the actual microstructure of the zinc coating. This method takes into account the individual orientations of the grains. This section also contains the numerical results of these finite element simulations.

2. Materials and method

The current study investigates three distinct steel substrates coated with identical Zn–Al–Mg coatings, all processed on the same galvanizing line. The first specimen (C_Mild) is a galvanized Mild steel sheet, the second (C_HSLA) is a galvanized High-Strength Low-Alloy steel (HSLA) sheet, and the last (C_Dual-Phase) is a galvanized Dual-Phase steel sheet, characterized by a heterogeneous microstructure composed of a soft ferritic matrix and hard martensitic islands providing a balanced combination of high strength and ductility. Both the Mild and the HSLA steel substrates exhibit the Lüders phenomenon with different Lüders plateau lengths at the beginning of the plastic flow. Table 1 provides details regarding the materials used in this study, and the chemical compositions of steel substrates are given in Table 2.

The average total coating weight for the Zn–Al–Mg coating is about 90 g/m^2 which corresponds to a coating thickness of about 7 μm. The galvanizing process is as follows. Steel sheets, produced from cold rolling, are transported to the galvanization line. The coils undergo a surface cleaning process to remove rolling oils, followed by a surface rinse, either chemically or electrochemically. Then, the sheet undergoes a metallurgical annealing process in a furnace at an annealing temperature up to 800 °C with a dry nitrogen and hydrogen atmosphere (5 to 20 vol% H2), with a controlled dew point. The surface iron oxides are reduced during this step to

Table 1. Characteristics of Zn–Al–Mg coated steel sheet samples investigated in the study: the coating alloy is the same for all three substrates

Sample label	Coating	Steel type	Substrate thickness (μm)	Coating thickness (μm)
C-Mild		Mild steel	2100	
C-HSLA	Zn–Al–Mg	HSLA	1200	7
C-Dual-phase		Dual-phase	1200	

Table 2. Chemical composition (wt%) of steel substrates

Element (wt%)	C	Si	Mn	Al	Cr	Phase
Mild steel	0.05	0.02	0.3	0.04	0.05	Ferritic
HSLA	0.08	0.25	1.6	0.06 max	-	Ferritic
Dual-phase	0.09	0.25	1.9	0.045	0.22	Dual-phase

expose the metallic surface to the molten zinc alloy, ensuring good adhesion between the sheet and the coating. Following the completion of the two primary surface preparation stages, the temperature of the sheet gradually decreases until it reaches the temperature of the zinc bath, which is approximately 460 °C. At this point, the sheet is immersed in the bath of molten zinc alloy for a brief duration, resulting in the formation of a liquid zinc layer as it emerges from the bath.

2.1. *Experimental protocol*

The microstructure of the materials was investigated by means of Field Emission Gun Scanning Electron Microscopy (FEG-SEM) using a JEOL IT800SHL and a FEI Nova NanoSEM 450. The crystallographic orientation of the grains in coatings was determined by Electron Backscatter Diffraction (EBSD) using an Oxford camera. To this end, the coating surface was ion polished during 20 min with 2 keV and 85° tilt on a Hitachi IM4000+ flat-milling machine. No mechanical polishing has been applied to the surface to avoid mechanical deformation of the coating. All the EBSD maps represent the orientation of the coating Normal Direction with respect to the single crystal axes. The red color indicates that the ND is parallel to the [0001] crystal direction.

Uniaxial tests were conducted using a ZwickRoell uniaxial tensile machine with a strain rate of 10^{-4} s^{-1}. Dog bone samples were extracted from galvanized sheets using laser cutting, with a gauge length of 60 mm (see the sample geometry in Figure 5a). The strain field on the coating surface was measured using the Digital Image Correlation (DIC) method. Before each test, the surface of the Zn–Al–Mg coating is first painted with a white background, and then a random speckle pattern is applied using black spray paint, enabling accurate measurement of the strain field. The system uses one camera with a resolution of 3048–3048 pixels, a focal length of 50 mm and an aperture of f/22. The stand-off distance is approximately 200 mm. The image scale is 2 μm/pixel. The acquisition rate is two images per second. The correlation analysis in the software uses a subset size of 27 pixels with a step size of 7 pixels. The calculated engineering strain fields are treated with a Gaussian spatial filter before analysing the results.

2.2. *Microstructure of the coatings*

Back-scattered electron (BSE) observations of the microstructures of the three specimens are presented in Figure 1. The coating is predominantly composed of proeutectic zinc dendrites, accounting for approximately 70% of the total area. Two eutectic phases are present in the

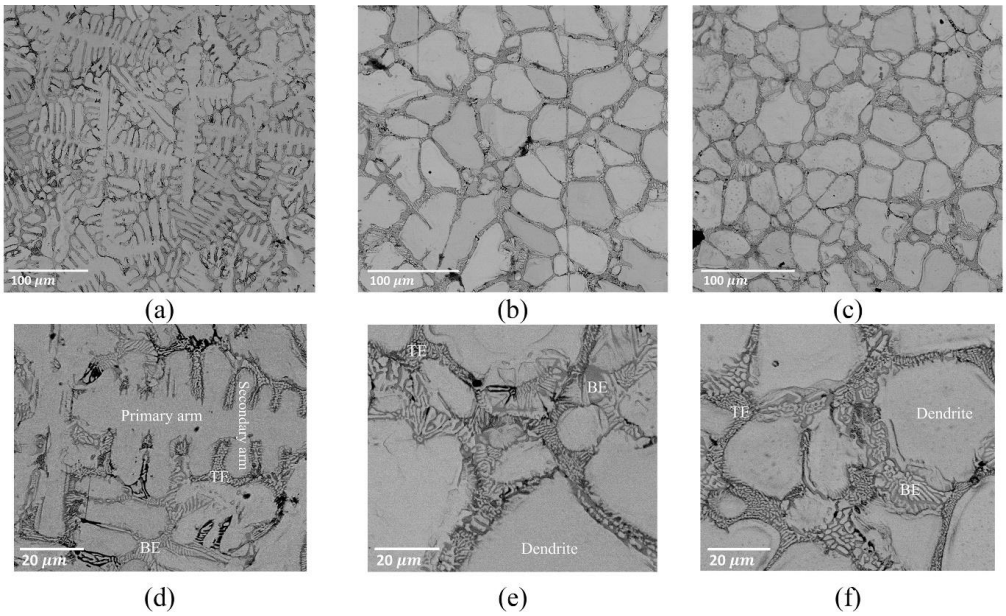

Figure 1. BSE-SEM micrographs at two different scales showing the different phases observed on the surface of (a,d) C_Mild, (b,e) C_HSLA, and (c,f) C_Dual-Phase.

remaining area: a coarse brittle binary eutectic Zn/MgZn2 (BE) and a thin ternary eutectic Zn/Al/MgZn2 (TE). The size and morphology of these dendrites are dependent by the underlying substrate. On the C_Mild specimen, the coating dendrites are two to three times larger than those on the C_HSLA and C_Dual-Phase, with an average size of 83 μm. Moreover, C_Mild dendrites exhibit distinct primary and secondary arms, while SEM images of C_HSLA and C_Dual-Phase reveal globular-shaped dendrites averaging 45 μm and 30 μm in size, respectively. Particularly, the coating deposited on dual-phase steel exhibits very small grains with diameters smaller than 10 μm, as depicted in Figure 1f.

In this part of the study, a qualitative description of the SEM observations is provided to highlight the relationship between the coating morphology and the nature of the substrate, rather than to suggest a direct influence of substrate grain size on dendrite shape.

2.3. *Crystallographic texture*

In addition to the dendrite morphology, the coating texture is influenced by the underlying substrate. The harmonic textures by pole figure (PF) are illustrated in Figure 2. Texture analysis is based only on the zinc phase (dendrite + zinc eutectic) which gives good indexation, except for the eutectic phase in some cases. This is due to the fact that eutectic phases are very thin (especially in the ternary eutectic). In the case of C_Mild, the coating surface displays both basal (0001) and prismatic ($1\underline{1}00$) or (1010) orientations (Figure 2a). On the other hand, the coating deposited on C_HSLA and C_Dual-Phase steel predominantly shows a high basal texture (0001) as demonstrated by the Figures 2b and 2c.

To understand the relationship between grain morphology and the underlying substrate, a comprehensive investigation was conducted using scanning transmission electron microscopy (STEM) analysis with a Jeol TEM instrument. The analysis focused on the interface between a Zn–Al–Mg coating and Mild and Dual-Phase steel. During the hot-dip galvanizing (HDG) process,

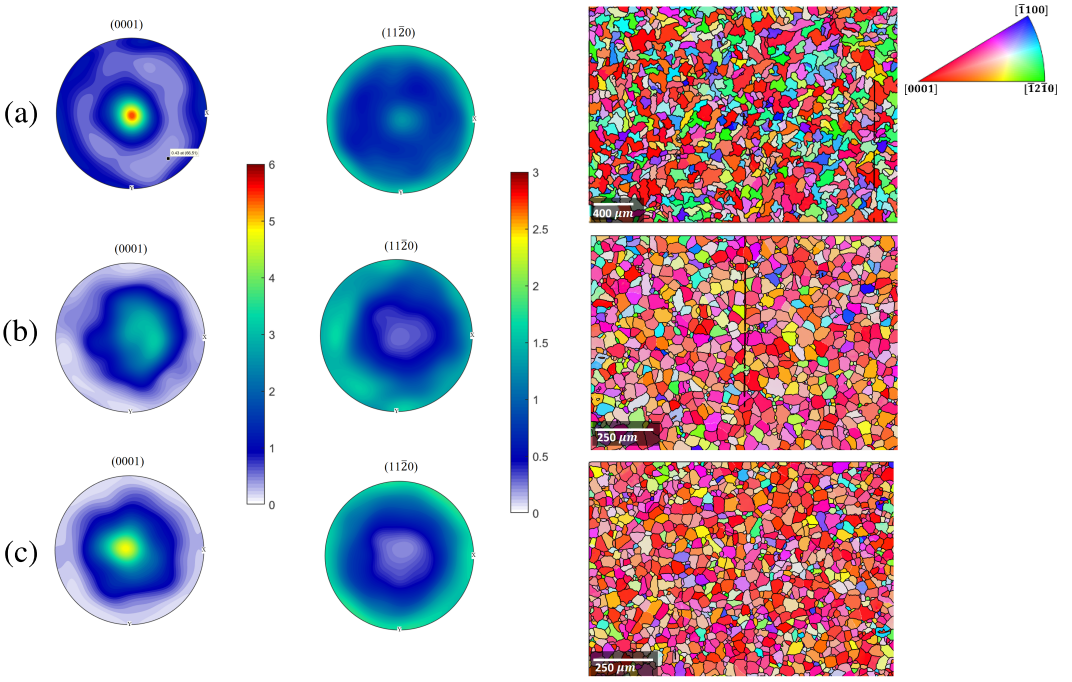

Figure 2. Direct pole figures in the RD-TD plane (left) and ND IPF maps (right) of the coatings on (a) C_Mild, (b) C_HSLA and (c) C_Dual-Phase substrates.

a well-defined Al-rich inhibition layer, denoted as $FeAl_3Zn_x$ or $Fe_2Al_5Zn_x$, was observed to form at the interface between the steel substrate and the coating [18–20]. This layer exhibits a uniform thickness of approximately 50 nm and plays a crucial role in preventing the formation of brittle FeZn compounds while significantly enhancing the overall adhesion of the coating.

Figure 3 presents the results of TEM analysis conducted on the coating/substrate interface of the C_Mild sample. In order to prepare a lamella for the analysis, a focused ion beam (FIB) method was employed, as depicted in Figure 3b. Moreover, Figure 3c showcases the STEM energy-dispersive X-ray spectroscopy (EDS) results obtained from a designated region (highlighted in Figure 3a) encompassing the secondary arm dendrite, binary eutectic phase, and ternary eutectic phase. The chemical composition analysis of the coating (Zn, Al, and Mg) presented in Figure 3c reveals that the binary eutectic phase, observed on the surface, extends all the way below the secondary zinc dendrite. Notably, an additional continuous layer consisting of aluminum has been observed at the interface of the coating and substrate, positioned beneath the binary eutectic and secondary arm dendrite phases. The chemical composition of the intermetallic layer rich in Al has been quantified utilizing the EDS technique by analyzing two regions. From the EDS analysis results, these regions rich in aluminum and iron were confirmed to be a $FeAl_3Zn_x$ intermetallic layer. A thickness between 60 and 200 nm has been measured for this layer.

The TEM analysis was extended to the second specimen C_Dual-Phase, which exhibited a distinct coating microstructure characterized by globular dendrites resembling that of the C_HSLA specimen (Figure 1b,c,e,f). This analysis revealed the presence of an intermetallic layer similar to the first specimen, with a binary eutectic phase extending below the zinc dendrite, as depicted in Figure 4c. Additionally, at the coating/substrate interface, a layer rich in manganese and silicon was observed. EDS local analysis, focusing on areas enriched in Mn and Si, as

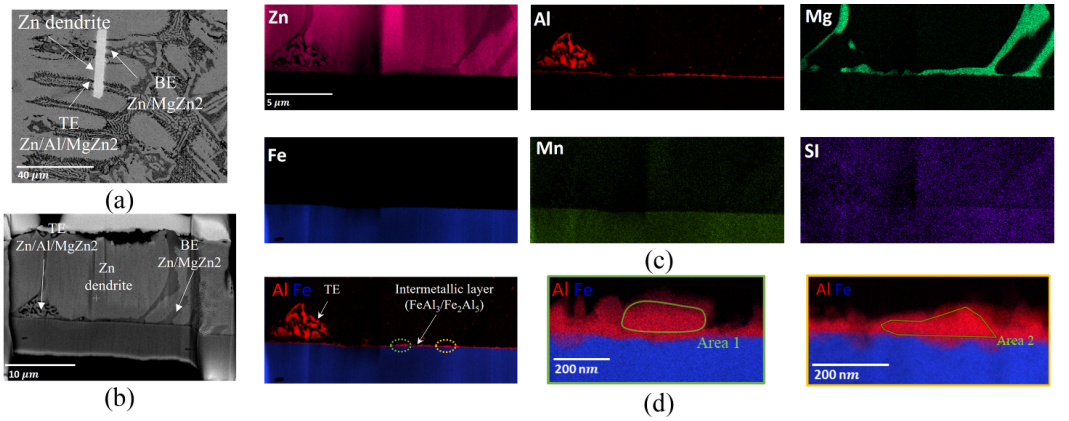

Figure 3. Intermetallic layer TEM analysis for C_Mild specimen: (a) deposited platinum on the location of the extracted STEM lamella including secondary zinc arm dendrite, binary eutectic phase and ternary eutectic phase, (b) the FIB extracted lamella, (c) chemical composition of the Zn–Al–Mg coating and the Mild substrate, (d) the chemical composition of the intermetallic at the interface.

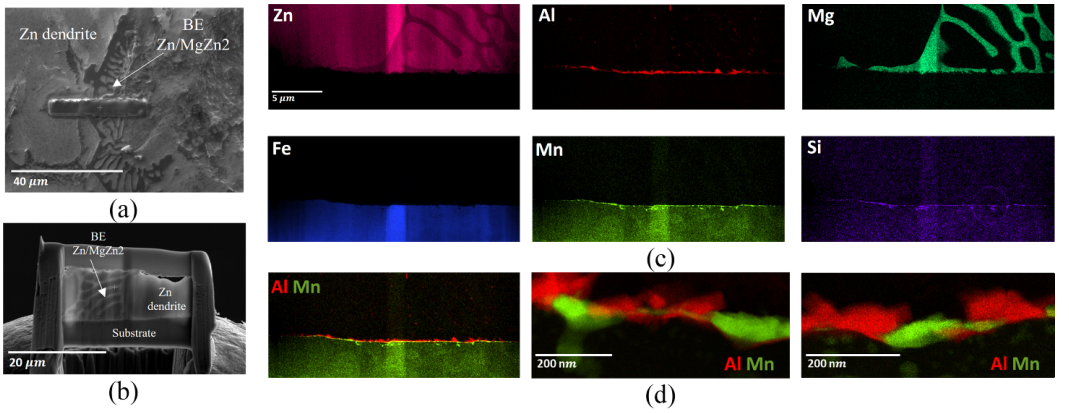

Figure 4. Intermetallic layer TEM analysis for C_Dual-Phase specimen, (a) Deposited platinum on the location of the extracted STEM lamella including zinc dendrite and binary eutectic phase, (b) the FIB extracted lamella, (c) chemical composition of the Zn–Al–Mg coating and the Dual-Phase substrate, (d) the chemical composition of the interface.

presented in Figure 4d, demonstrated that this layer primarily consists of MnO and Mn_2SiO_4 oxides. This external oxide layer is commonly known as selective oxidation and is frequently observed in steels containing significant amounts of Mn and Si [21]. Some of these oxides are observed within the superficial layer of the substrate at the grain boundaries. Notably, the local analysis specifically targeting this oxide layer revealed that the formation of the intermetallic layer FeAl3 was impeded in the presence of MnO and Mn_2SiO_4 oxides.

The presence of the oxide layer, composed primarily of MnO and Mn_2SiO_4 oxides, at the interface between the steel substrate and the Zn–Al–Mg coating can influence the microstructure of the coating. This oxide layer may have an impact on grain morphology and size within the coating. The interaction between the oxides and the coating material could lead to alterations in the nucleation and growth of grains, potentially resulting in changes to the overall microstructural

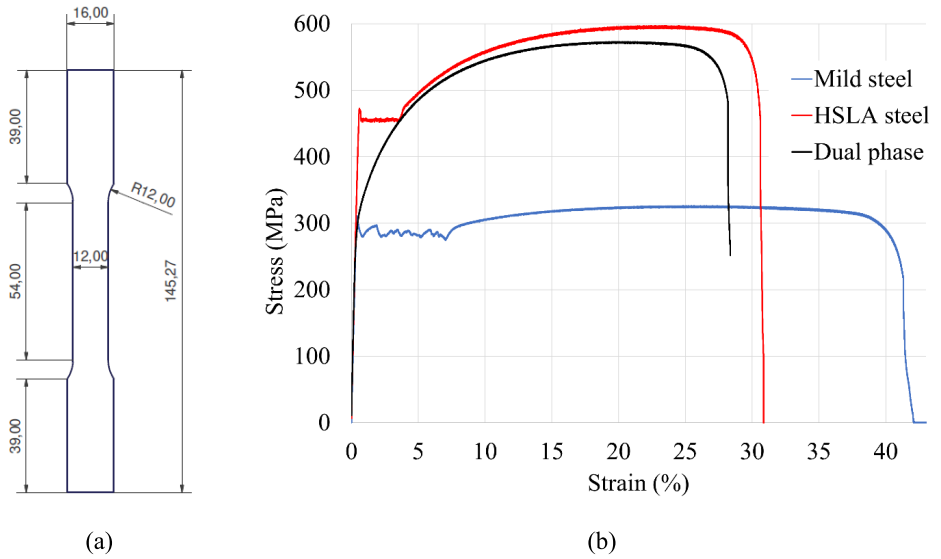

Figure 5. (a) Sample geometry, (b) engineering stress–strain responses during uniaxial tensile tests of C_Mild, C_HSLA, and C_Dual-Phase steels.

characteristics. Further studies are currently underway to explore in greater detail the impact of these oxides on the germination and growth of zinc grains.

3. Deformation modes of the coatings

In addition to the observed differences in coating microstructure and crystallography, as discussed in Sections 2.1 and 2.2, it is important to recognize that the mechanical behavior of the underlying substrate can profoundly impact the deformation characteristics of the Zn–Al–Mg coating. In this section, the deformation behavior is analysed in function of the coating microstructure and crystallography, the steel behavior and the loading mode.

3.1. *Macroscopic uniaxial tensile tests*

Uniaxial tensile tests were performed on C_Mild, C_HSLA, and C_Dual-Phase coated steels at various strain levels to examine the local plasticity behavior of the Zn–Al–Mg coating. Figure 5 illustrates the macroscopic behavior observed in these tests. Notably, as shown in Figure 5, the plastic deformation responses of the studied samples exhibit significant differences. It is important to note that the relatively thicker substrates have a more prominent influence on the observed global mechanical properties, predominantly reflecting the plastic deformation tendencies of the substrates rather than the coatings themselves. In the case of the coatings on Mild and HSLA substrates, a discontinuous yielding behavior characterized by Lüders peak and plateau stresses is observed, occurring after the initial elastic regime. The length of the Lüders plateau is found to be 8% and 3.5% for the C_Mild and C_HSLA steels, respectively. Conversely, the samples with the Dual-Phase substrate demonstrate continuous yielding behavior without the presence of Lüders bands.

DIC measurements conducted on the surfaces of C_Mild and C_HSLA specimens, as depicted in Figures 6a and 6b respectively, reveal the presence of strain localization at the initial stages

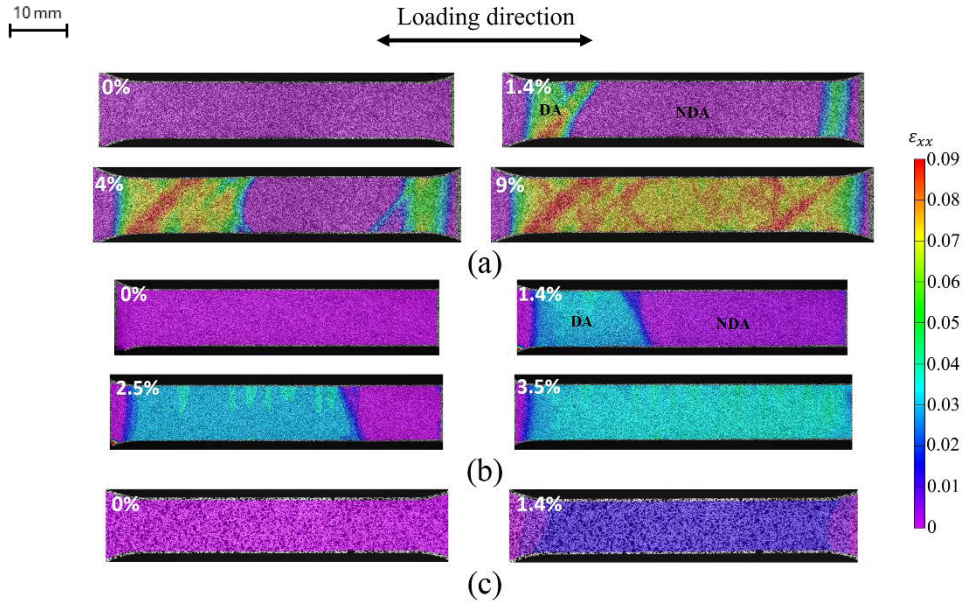

Figure 6. Local horizontal engineering strain distributions along the gauge length of the specimens, obtained using digital image correlation (DIC) during uniaxial tensile tests: (a) position of Lüders bands at different levels of macroscopic applied strain for the C_Mild steel specimen, (b) position of Lüders bands at different levels of macroscopic applied strain for the C_HSLA steel specimen, and (c) strain field distribution at different levels of macroscopic applied strain for the C_Dual-Phase steel specimen.

of loading. At a macroscopic strain of 1.4%, two non-homogeneous bands with localized deformation spanning between 6% and 8% appear at the edge of the gauge area in the C_Mild specimen. These bands gradually encompass half of the specimen after 4% of macroscopic strain and eventually propagate across the entire useful cross-sectional area by 8% macroscopic strain. In the case of the C_HSLA steel, a Lüders band with a magnitude of 3.5% is measured at a macroscopic strain of 1.4%, initially occupying almost half of the gauge length. As the macroscopic strain reaches 3.5%, this band expands to cover the entire gauge length. Before the band propagates to the entire specimen, two distinct areas can be identified within the gauge section: a plastically Deformed Area (DA) and a plastically Non-Deformed Area (NDE), as depicted in Figures 6a and 6b at a macroscopic strain of 0.014. In contrast, for the last specimen, C_Dual-Phase, which does not exhibit Lüders effects on the tensile curve, no strain localization is observed at the gauge length of the uniaxial tensile specimen, indicating a homogeneous mechanical behavior (Figure 6c). In the remainder of the article, all SEM analyses presented in the following sections were conducted in the DAs.

Lüders band formation is a material instability which can occur in principle at any location of the steel sample. Stress concentration points, such as the width transition zone of the sample, may act as perturbations of the field and trigger the band initiation. This is indeed the case in the experiments of Figure 6. However, this is not always the case in Lüders experiments.

3.2. *Deformation modes*

Before studying the effect of Lüders banding on the deformation behavior of the zinc coating, the principal deformation modes of individual grains are investigated. Figure 7 shows a SEM

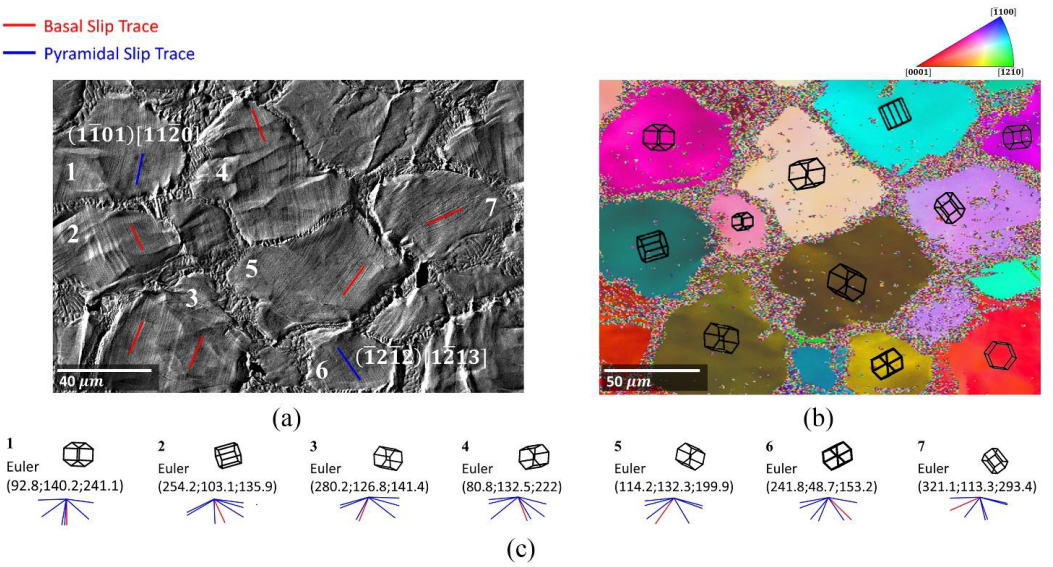

Figure 7. (a) SEM micrograph of C_Dual_phase specimen after tensile loading at a strain value of 0.07; (b) the corresponding IPF map; (c) possible slip trace directions in selected grains.

micrograph and an IPF map of the same zone for the C_Dual-Phase specimen deformed at 0.07 strain level. The plastic deformation within the zinc grains can be observed through several means. Firstly, slip traces of different slip families within the grains can be visualized in SEM images, as shown in Figure 7a. Additionally, orientation gradients on the IPF (Inverse Pole Figure) map, as depicted in Figure 7b, provide further evidence of plastic deformation occurring within the zinc grains. Slip trace analysis reveals that basal slip (0001) and 2nd order pyramidal slip, indicated by red and blue lines on Figure 7a, respectively, are the dominant modes of slip deformation within the zinc grains (Figure 7c).

Furthermore, IPF maps of the uniaxial tests presented in Figure 8 demonstrate that for high enough applied strain, twinning emerges as the primary deformation mode within some zinc grains. This twinning mechanism plays a crucial role in redistributing stress and facilitating the plastic deformation of the grains under such conditions.

To investigate the influence of Lüders bands on plasticity within zinc grains, EBSD analyses were conducted on all specimens after applying an uniaxial macroscopic strain of 0.014. For each specimen, an area containing approximately 60 grains in the DA zone was analyzed. Figure 8 presents the IPF maps and the GND (Geometrically Necessary Dislocation) of the deformed area. The GND maps were calculated using the AZtecCrystal software® from Oxford, employing the "Weighted Burgers Vector" (WBV) technique. Dislocation density was calculated utilizing the basal slip system (0001) and the pyramidal slip system $(1\underline{1}01)$ and $(1\underline{2}1\underline{2})$. In addition, the quantification of the twinned area fraction within the selected grains was also performed using the same AZtecCrystal software, based on the automatic identification of twin orientation relationships.

In the deformed area, in Figure 6, the C_Mild specimen exhibits a significant amount of plastic strain, as evidenced by numerous twinning bands within the zinc grains (Figure 8a). Some of these twins have already invaded almost the entire grain, indicating extensive plastic deformation. Note that the twin shear value in zinc is 0.139. Moreover, several twinning systems can coexist in the same grain. The newly oriented twinned grains can experience further

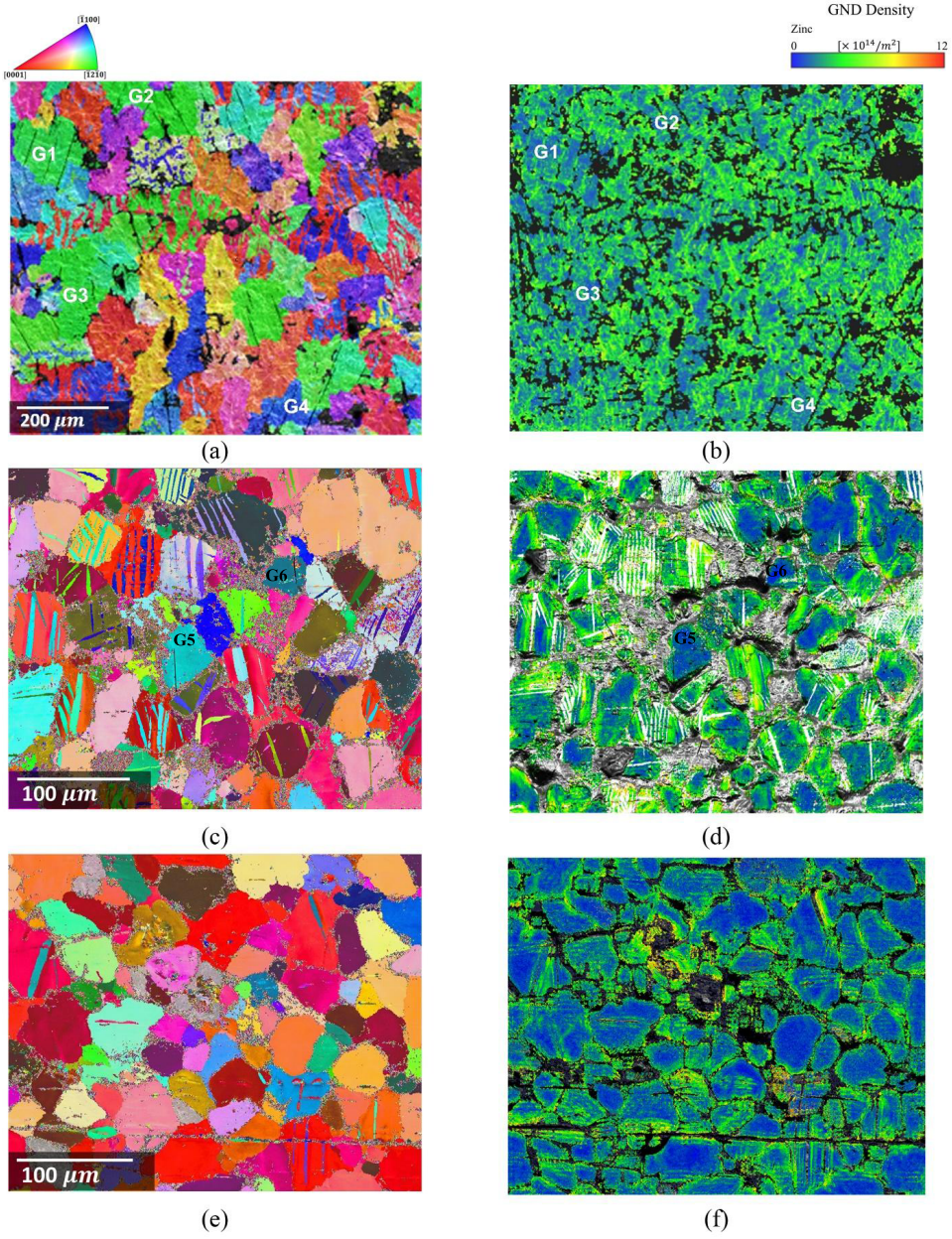

Figure 8. ND IPF_Z and GND maps of (a,b) C_Mild, (c,d) C_HSLA and (e,f) C_Dual-Phase steel specimens after 0.014 of major strain during uniaxial tensile tests.

plastic deformation through slip activity, as evidenced by a visible orientation gradient inside the twinned area shown in Figure 8a. Additionally, twinning is highly prevalent in grains oriented with their *c*-axis perpendicular to the sheet plane. Twinned grains represent approximately 50% of the observed area, illustrating the significance of this deformation mechanism. Figure 8b presents the dislocation density of the deformed area of the C_Mild specimen. Interestingly, the dislocation density of grains with *c*-axis lying on the sheet surface is lower than that of grains with other orientations. This is demonstrated in G1, G2, G3, and G4 grains with $(1\underline{1}00)$ orientation.

While not shown here, no extensive plasticity was found in the Non-Deformed Area, confirming that significant plasticity development only occurs due to the passage of the Lüders bands.

In the case of the C_HSLA specimen, similar deformation modes to those seen in the C_Mild specimen were observed. Twinning emerged as the principal deformation mode, with approximately 65% of twinned grains in the deformed area after a macroscopic strain of 0.014, corresponding to a local strain of 0.035 within the DA. At this strain level, multiple twins formed within the zinc grains and began thickening. The high percentage of twinning can be attributed to the crystallographic orientation difference between the C_Mild and C_HSLA steel specimens. As mentioned in Section 2.2, basal orientation is prevalent in C_HSLA steel, leading to an increased occurrence of twinning compared to C_Mild specimens, where twinning primarily occurred in grains with *c*-axis parallel to the Normal Direction of the steel surface (ND). However, the twin area fraction inside the grains in C_HSLA remains significantly lower than that in C_Mild specimens, despite its grain size being twice smaller. This difference can be attributed to the local strain being twice higher in C_Mild specimens (8% against 3.5%). The GND map in Figure 8d illustrates a high dislocation density in grains where twinning is prevalent. Conversely, other grains do not exhibit significant plasticity, irrespective of their crystallographic orientation.

As for the final C_Dual-Phase specimen depicted in Figure 8e, out of the same number of investigated grains as the previous two specimens, only 6% began to twin, and the fraction of twin area was very low despite the favourable grain orientation to twinning. Moreover, the GND map presented in Figure 8f demonstrates only a minor amount of plasticity inside the zinc grains. This is due to the low applied macroscopic strain, 0.014, distributed uniformly, in the absence of Lüders banding.

3.3. *Cracking modes*

Cracking modes of the coatings have been observed for all materials at several strain levels for uniaxial tests. Figure 9 shows cracking modes of C_Mild, C_HSLA and C_Dual-Phase steel during uniaxial tests at a macroscopic strain of 0.014, corresponding to the areas shown in Figure 8.

In Figure 9a, a significant number of cracks can be observed traversing the zinc grains. To be specific, the grains designated as G1, G2, G3, and G4, which are highlighted in both Figures 8a and 9a, serve as typical examples that nearly all grains with their *c*-axis oriented parallel to the sheet plane display multiple instances of cleavage cracking. Some cleavage cracks are also observed on the C_HSLA specimen in grains with similar orientation (G5 and G6), as shown in Figures 8c and 9c. Microcracks in the brittle binary eutectic phase are also observed in both C_Mild and C_HSLA specimens. Conversely, no cleavage cracking is evident in the C_Dual-Phase specimen, despite the presence of grains with *c*-axis alignment parallel to the sheet plane. This discrepancy can be attributed, firstly, to the textural differences in the coating of C_HSLA and C_Dual-Phase steel, and secondly, to the lower strain levels in comparison to the C_Mild specimen. Notably, for the C_Dual-Phase specimen, the applied macroscopic strain remains low and insufficient to induce any surface coating damage.

4. Modeling and simulation

In this section, the three-dimensional mechanical behavior of zinc coatings deposited on steel substrates is simulated by means of the crystal plasticity finite element method. This computational endeavor is aimed at gaining deeper insights into the complex interplay between the coating and the substrate under various mechanical loading scenarios. The simulation adopts an advanced crystal plasticity model for the coating and an isotropic von Mises plasticity model for the substrate by modeling the Lüders plateau and its effect on the coating behavior. The computational approach initiated in [15,17] is extended here to the large deformation

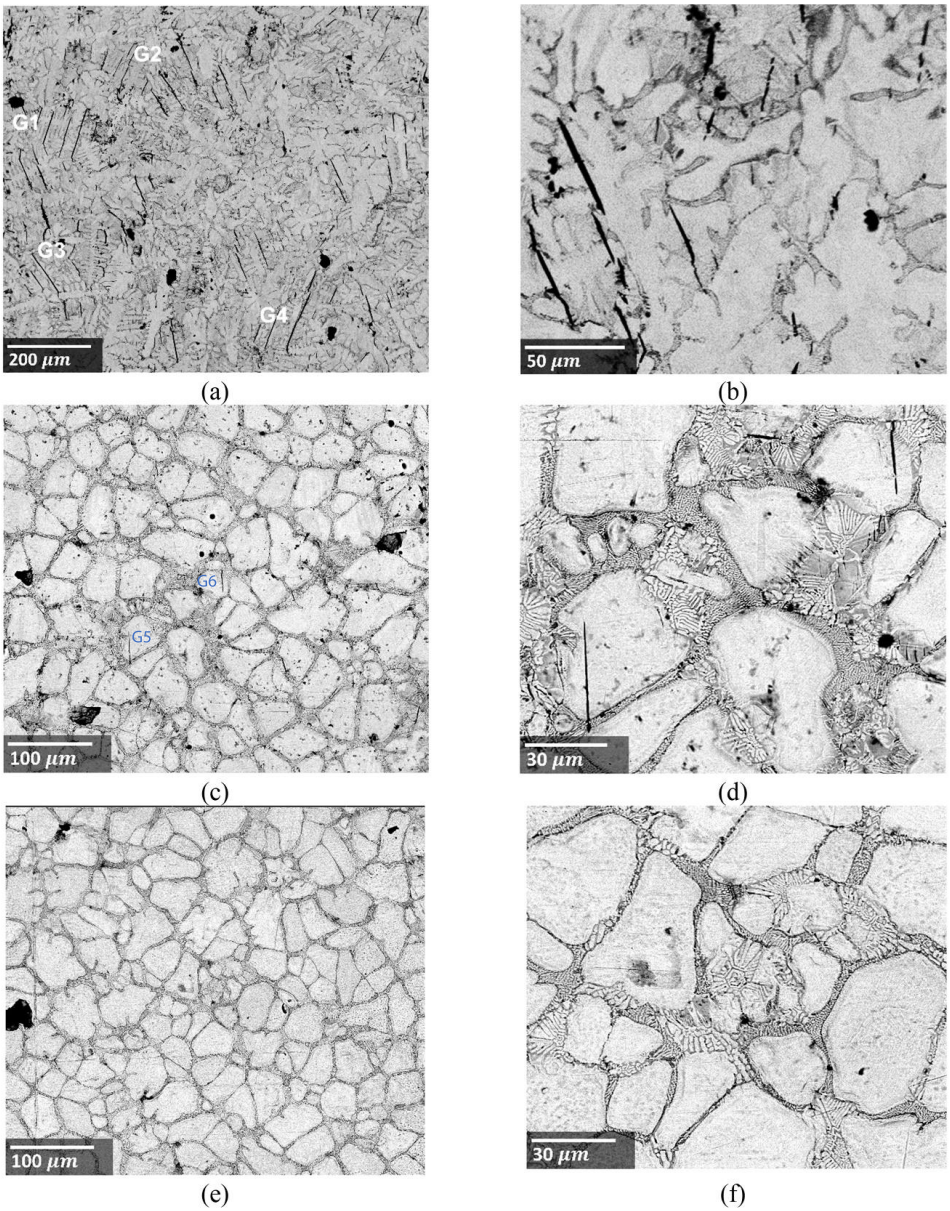

Figure 9. BSE-SEM images showing selected coating surface areas presented in Figure 8 of (a,b) C_Mild, (c,d) C_HSLA, and (e,f) C_Dual-Phase specimens deformed up to 0.014 of global strain.

crystal plasticity framework and applied to the three considered combinations of steel substrates and coating systems.

4.1. *Simulation method*

The approach referred to as the "multicrystalline approach" intricately considers the actual geometry and orientation of zinc grains in the coating. Given the inherently complex multiphase

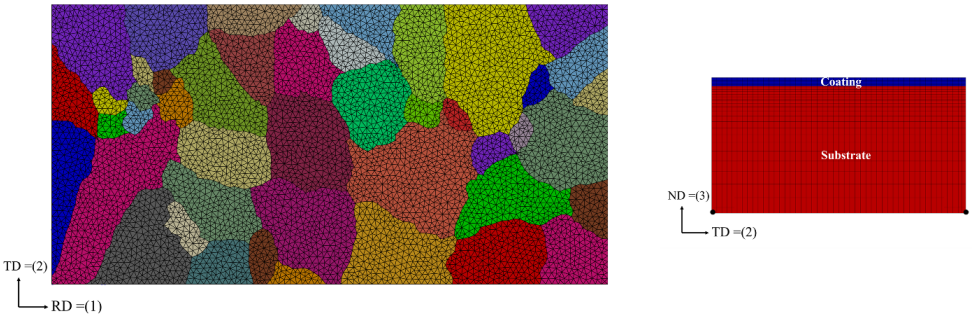

Figure 10. Example of a finite element mesh of a tensile specimen, (a) free coating surface and (b) coating/substrate cross-section.

microstructure of the Zn–Al–Mg coating, it becomes imperative to consider the various morphologies when generating the finite element (FE) mesh. Additionally, the orientations of these grains play a pivotal role in determining the mechanical response of the coatings, as shown in Section 3, and must be incorporated into the material model. This approach, initiated in reference [22], makes use of the real coating microstructure obtained from EBSD analysis to create a realistic mesh that encompasses both the microstructure and the orientations of grains.

The data obtained from the EBSD analysis is initially processed using the MTEX toolbox [23], specifically designed for Matlab. Subsequently, the MTEX2Gmsh tools, developed by [24], are employed to generate 2D meshes from the EBSD data, utilizing the features of the MTEX toolbox. The generated geometry file is further refined using Gmsh software [25] allowing control over mesh density. An example of final mesh is given in Figure 10. In this study, to simplify the calculations, we opted to include only the zinc phase in the model, thus including the eutectic phases into the neighboring grains according to the epitaxy orientation relationships.

To extend this two-dimensional mesh into a three-dimensional representation, a straightforward translation along the Normal Direction (ND) is applied, since grain boundaries are perpendicular to the sheet plane, with a good approximation. The coating is monocrystalline throughout the thickness, as illustrated in Figures 2b and 3b. Each grain in the coating has a specific label (ID number) which defines a set of elements which a triplet of Euler angles is attributed (Figure 10a).

The substrate is meshed by translating the same two-dimensional coating mesh but with varying thickness. In the thickness direction, the coating is segmented into six layers of regular elements while a progressive meshing is used for the substrate, with elements identical to the coating near the interface and coarser far from the interface (Figure 10b). The final step is the conversion of the mesh to a geometry file that is recognized by the finite element software Z-set.

In this simulation, we employed finite elements with quadratic interpolation functions and reduced integration points to achieve accurate results. Table 3 provides details regarding the number of brick elements, integration points, and nodes for each specimen, ensuring that mesh was properly refined for numerical precision of the computed fields. Note that the fine meshes used in this work lead to a large number of unknown degrees of freedom (dof), close to 3 million dofs. The implicit resolution of the problem requires a large amount of memory and was distributed over 10 processors. Long simulation times (typically one week) were necessary to simulate the tensile tests. The strain localization phenomenon associated with Lüders band initiation and propagation leads to fine time steps in the simulation. The Newton implicit method is used for both the resolution of global static equilibrium and the resolution of the differential system of constitutive equations at each Gauss point.

Table 3. Mesh details for simulated specimens

	Nodes	Elements
C_Mild steel	987 103	380 160
C_HSLA steel	779 501	298 064
C_Dual-phase steel	737 367	283 030

Continuity of the displacement vector (no crack nor slip) and of the traction vector are assumed at the interface.

The following boundary conditions have been applied to simulate tension in rolling direction 1 (RD) and to allow for the formation of Lüders banding (Figure 10a). A vanishing displacement $U_1 = 0$ is applied to all nodes of the surface $x_1 = 0$ (substrate and coating, left side in Figure 10). The displacement component U_1 is prescribed to the nodes of the surface $x_1 = L$, L being the length of the meshed plate (right side in Figure 10a), with a constant displacement rate corresponding to the loading rate of the experiment. All the lateral surfaces normal to TD and ND (including the coating free surface and the bottom steel surface) are left free of forces. In that way, the Lüders band can propagate without boundary kinematical constraints, except at the specimen's ends which remain flat due to the prescription of the U_1 displacement component. Appropriate additional displacements are applied to fix the rigid body motion (not detailed here).

The microstructure of the coating, which was studied experimentally through uniaxial tests, is now simulated in this section, with the results detailing the local deformation behavior. Figure 11 presents the EBSD maps of each specimen, with grain numbers assigned after preparation using the MTEX toolbox. Notably, the C_Dual-Phase specimen exhibits a significantly higher grain density compared to the C_HSLA specimen. This difference arises from the presence of very small grains, as depicted in Figure 1c. To ensure consistency, a larger surface area was considered for the C_Mild specimen to achieve a similar number of grains compared to the C_HSLA specimen.

4.2. *Steel sheet behavior*

The mechanical behavior of the steel sheets used in this study has been identified from the tensile tests performed in the rolling direction (RD), as presented in Section 3. The plasticity law of the steel sheets is based on a Mises yield criterion, as expressed in Equation (1). An isotropic nonlinear hardening model has been adopted to describe the evolution of the yield stress as a function of the cumulative plastic strain, denoted as p. In this work, the materials are considered isotropic, and the constitutive model does not account for potential anisotropy that could result from the manufacturing process, particularly from the rolling operations. However, the DIC measurements provide information on the Lankford coefficient for the lateral strain during tension along RD, which was found compatible with isotropy.

For the Dual-Phase steel substrate the hardening law is given by Equation (2) while the hardening law for Mild and HSLA steel substrates is given by Equation (3). In the hardening laws, R_0 represents the initial yield stress, while Q_1, Q_2, Q_3, b_1, b_2, and b_3 are material parameters characterizing the exponential functions describing the hardening behavior. The equation incorporates a classic Voce strain hardening behavior in its initial part [26,27]. To account for the Lüders effect and associated strain localization observed during the experimental tests, attributed to dislocation anchoring and release, we introduce an additional softening term with a negative coefficient Q_2. The third additional hardening Q_3 term is employed to smooth out the initial peak in the local material behavior and enhance convergence in finite element calculations. Figure 12

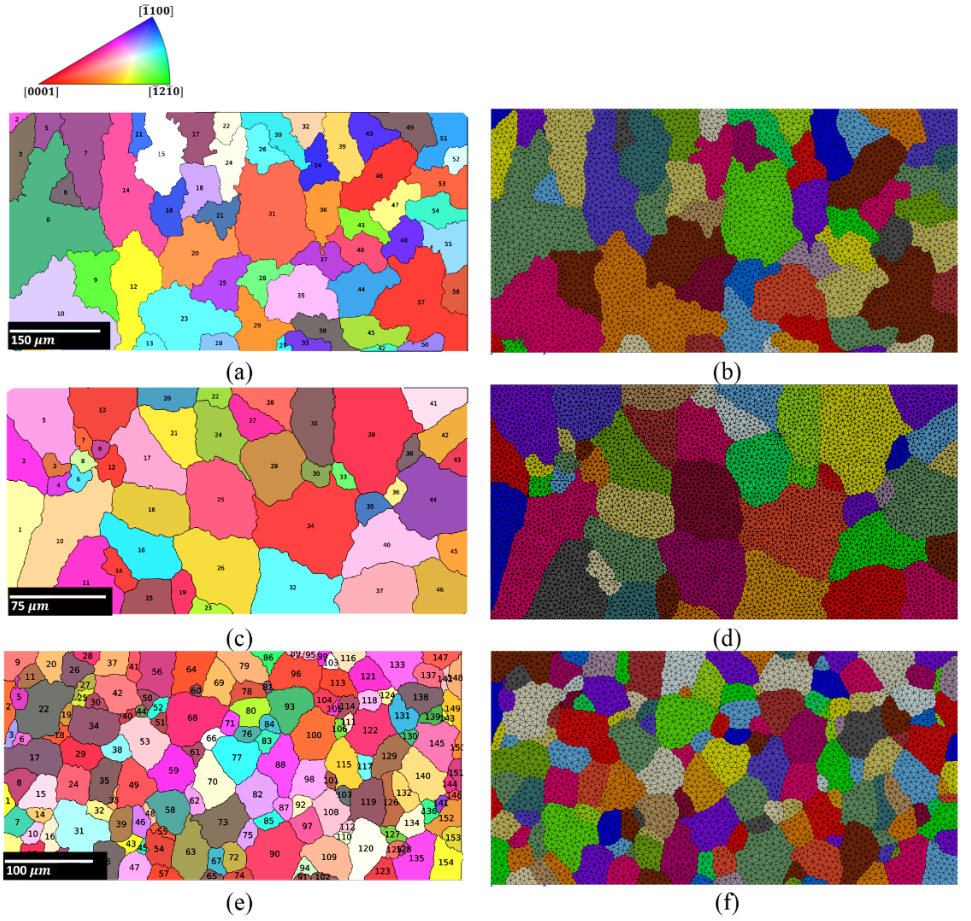

Figure 11. EBSD maps with the associate finite elements mesh for the (a,b) C_Mild steel specimen, (c,d) C_HSLA steel specimen and (e,f) C_Dual-Phase steel specimen: grain numbers and orientations on the left and finite element mesh of the coating surface.

gives the comparison between the experiments and the simulation of steel sheets in rolling direction.

$$f = (\frac{1}{2}[(\sigma_{11}-\sigma_{22})^2+(\sigma_2-\sigma_{33})^2+(\sigma_{33}-\sigma_{11})^2+6(\sigma_{23}^2+\sigma_{31}^2+\sigma_{12}^2)])^{0.5}-R \quad (1)$$

$$R = R_0 + Q_1(1-\exp(-b_1 p)) + Q_2(1-\exp(-b_2 p)) \quad (2)$$

$$R = R_0 + Q_1(1-\exp(-b_1 p)) + Q_2(1-\exp(-b_2 p)) + Q_3(1-\exp(-b_3 p)) \quad (3)$$

The hardening parameters identified for the Mild steel substrate are reported below. These values were obtained from the tensile tests in the rolling direction and fitted using Equation (3). The identified parameters are: $R_0 = 310$ MPa, $Q_1 = 140$ MPa, $b_1 = 2.6$, $Q_2 = -65$ MPa, $b_2 = 110$ and $Q_3 = 150$ MPa with $b_3 = 1.5$.

4.3. *Coating behavior*

To simulate the mechanical behavior of the zinc coating, a crystal plasticity finite deformation model with the multiplicative decomposition of the deformation gradient has been employed.

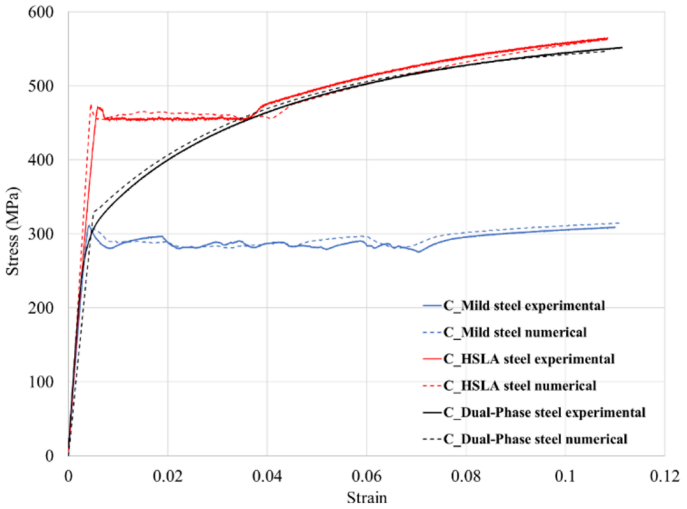

Figure 12. Global mechanical responses of experiment and coating/substrate FE simulation for C_Mild, C_HSLA and C_Dual-Phase steel specimens during uniaxial tensile tests.

The multiplicative decomposition of the deformation gradient into an elastic part F^e and an inelastic part F^p is written in Equation (4).

We define the velocity gradient tensor L as the sum of the contributions of all activated slip systems Equation (5) with $\dot{\gamma}^s$ being the slip rate for the slip system s. It is recalled that the slip direction and normal to the slip plane are denoted by m^s and n^s, respectively. The total number of considered slip systems is N_s. The criterion for the activation of slip system s is the Schmid law given in Equation (6). The viscoplastic Norton-type flow law is also given by Equation (6). A cumulative slip variable is introduced by Equation (7).

The Critical Resolved Shear Stress (CRSS) is given by Equation (8) where M is the Mandel stress tensor defined by Equation (9) with Π^e is the second Piola–Kirchhoff stress tensor with respect to the intermediate configuration. The isotropic strain hardening law is given by Equation (11). It involves an interaction matrix coupling the slip systems of various families.

$$\underset{\sim}{F} = \underset{\sim}{F}^e \underset{\sim}{F}^p \tag{4}$$

$$\overline{\underset{\sim}{L}}^p = \underset{\sim}{\dot{F}}^p \underset{\sim}{F}^{p-1} = \sum_s^{N_s} \dot{\gamma}^s (m^s \otimes n^s) \tag{5}$$

$$\dot{\gamma}^s = \text{sign}\,(\tau^s) \left\langle \frac{|\tau^s| - \tau_0^s}{K^s} \right\rangle^{n^s} \tag{6}$$

$$\dot{\gamma}^s_{\text{cum}} = |\dot{\gamma}^s| \tag{7}$$

$$\tau^s = \underset{\sim}{M} : m^s \otimes n^s \tag{8}$$

$$\underset{\sim}{M} = J_e \underset{\sim}{F}^{eT} \cdot \underset{\sim}{\sigma} \cdot \underset{\sim}{F}^{e-T} = \underset{\sim}{C}^e \cdot \underset{\sim}{\Pi}^e \tag{9}$$

$$\underset{\sim}{C}^e = \underset{\sim}{F}^{eT} \underset{\sim}{F}^e \tag{10}$$

$$\tau_c^s = \tau_{0c}^s + \sum_{r=1}^{N} Q^s h_{rs} (1 - \exp(-b_r \gamma^r_{\text{cum}})) \tag{11}$$

The material parameters τ^s_{0c}, Q^s, h_{rs}, K^s and n^s were identified by [15,28] for the basal, pyramidal P1 and P2, and prismatic slip-system families of single-crystalline zinc. Twinning is modeled as a pseudo slip system and does not consider the lattice orientation change in the twinned phase.

The reader is referred to [15] for a detailed description of the interaction matrix and identification procedure. In particular, the viscosity parameters K^s and n^s account for the rate-dependent behavior of zinc at room temperature.

In the following results, the plastic shear strain is assumed to occur solely on the 15 HCP slip systems, 3 basal systems $\{0001\}\langle 11\underline{2}\rangle$, 6 pyramidal π_2 systems $\{1122\}\langle 11\underline{2}3\rangle$ and 6 twinning system $\{10\underline{1}2\}\langle 10\underline{1}1\rangle$ characterized by the slip directions m^s and the normal to the slip planes n^s. This choice was based on experimental observation of slip systems shown in Figure 7 and EBSD analysis presented in Figure 8.

4.4. *Numerical results and comparison with experiments*

To offer a comprehensive insight into the mechanical behavior, we present the distribution of slip activity in each grain within the coating and strain component F_{11} along the tensile direction within both the coating and the steel substrates. Figures 13, 14 and 15 provide a visual representation of the strain distribution at various loading stages and across cross-sectional layers for the C_Mild, C_HSLA and C_Dual-Phase steel specimen, respectively. The component F11-1 coincides with the horizontal engineering strain component plotted in Figure 6. They illustrate the propagation of the Lüders band through the substrate and its interaction with the coating.

The fields are represented at three different locations in Figures 13–15. The surface DN = 0 represents the layer of Gauss integration points at the bottom of the substrate in Figure 5 and therefore characterizes the bulk steel response. The name "interface" in the captions refers to the first layer of Gauss integration points just above the interface, on the coating side. The surface DN = 1 denotes the first layer of Gauss integration points just below the free surface of the coating. Information is taken at the Gauss points because node values for stress and strains are generally not continuous at grain boundaries and at the substrate/coating interface.

In the simulations of the Lüders behavior, the width transition zones in tensile specimens play a similar role in band triggering as in the experiment, see the macroscopic simulations in [26]. However, in the present simulations of polycrystalline coatings on a substrate, the width transition zones were not included in the finite element mesh because only a small part of the gauge length could be considered. The bands are observed to start from the left end of the mesh in Figure 13, probably due to stress concentrations induced by the boundary conditions (imposed axial displacement) in the coating grains and transmitted to the substrate.

Figures 13a and 13b show the local strain F_{11} at the bottom steel surface (ND = 0) of the Mild steel. These pictures capture the state of F_{11} at two 2% and 4% of applied macroscopic strain. The corresponding local strains at the bottom steel surfaces of the C_HSLA and C_Dual-Phase steel specimens are presented in Figures 14a,b, and 15a,b, respectively.

Upon reaching a macroscopic strain of 2%, the Dual-Phase steel exhibits a uniform strain field, matching the magnitude of the applied macroscopic strain. In contrast, both Mild and HSLA steel show the initiation of a Lüders band on the left side, traversing a portion of the plate and leading to the development of heterogeneous strain. Furthermore, the local strain in the Mild and HSLA steels is respectively four times and two times greater than that observed in Dual-Phase steel at the same macroscopic strain. This local plastic strain correlates in magnitude to the length of the Lüders plateau. For a macroscopic strain of 4%, the strain field within the Dual-Phase steel specimen remains uniform on the bottom surface, with the magnitude aligning precisely with the applied strain, as shown in Figure 15b. In contrast, for the HSLA steel, the Lüders band propagated along the entire specimen (Figure 14b). In the case of the Mild steel, shown in Figure 13b, it spans only half of the specimen's length. This difference is due to the length of the Lüders plateau, which is twice as long in Mild steel as in HSLA steel.

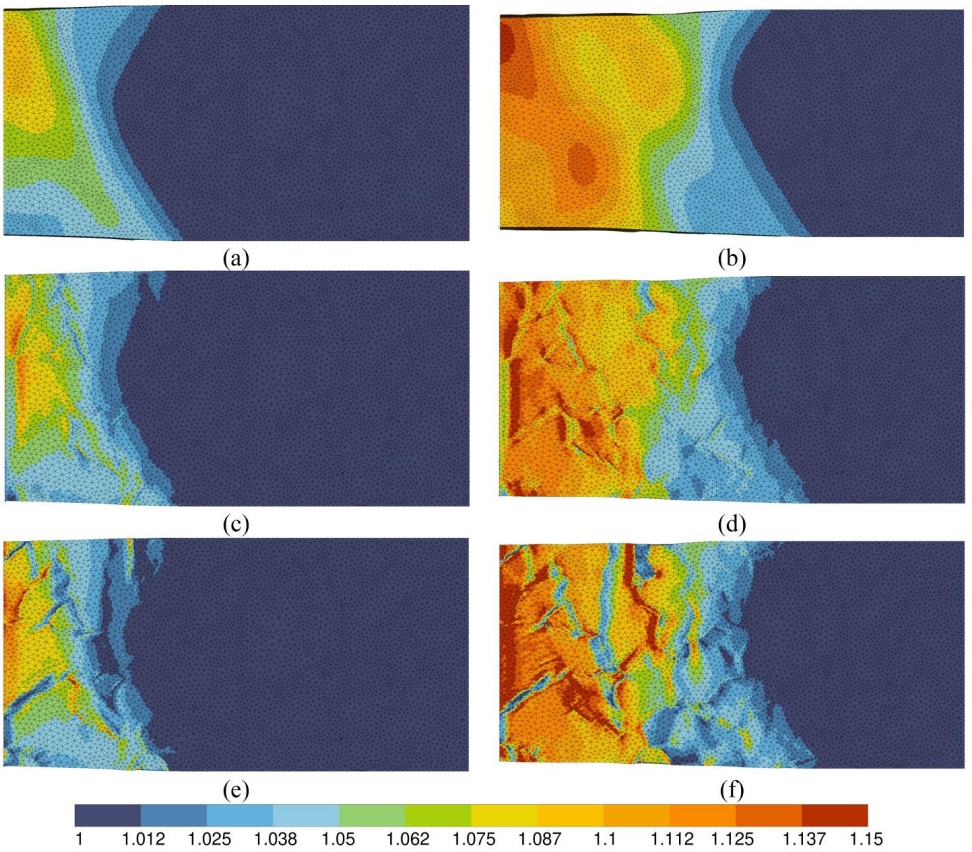

Figure 13. Distribution of the strain component F_{11} along the tensile axis for the C_Mild steel specimen at overall strain levels 2% (left) and 4% (right): (a,b) at the substrate surface (ND = 0), (c,d) at the interface and (e,f) at the coating surface (ND = 1).

The distribution of the strain component $F_{11} = 1 + \varepsilon_{11}$ along the tensile axis at the coating surface (ND = 1), at various loading stages, is presented in Figures 13e,f, 14e,f and 15e,f, corresponding to the C_Mild, C_HSLA, and C_Dual-Phase steel specimens, respectively. These strain maps are complemented by maps of plastic activity in the coating in Figures 16–18 where plastic activity is represented by the sum of cumulative plastic slip amounts for each system family (basal, pyramidal and twinning). In the case of the C_Dual-Phase specimen, as depicted in Figure 15e, following the application of macroscopic strains of 2% and 4%, the local strain F_{11} exhibits remarkable uniformity within each grain. This uniformity is primarily attributed to the strain imposed by the underlying substrate. It is worth noting that certain grains within this specimen do not undergo plastic deformation and thus remain in an elastic state. Within the deformed grains, however, there exists a significant heterogeneity in plastic strain from one grain to another, see Figures 18a and 18c. This variation is particularly pronounced at grain boundaries, where peaks of slip activity are concentrated. This phenomenon is the result of the plastic-strain incompatibility between neighboring grains and is further influenced by the strong elastic anisotropy of zinc, especially during the initial stages of plastic deformation.

In the case of the C_Mild and C_HSLA specimens, applying the same macroscopic strain leads to substantial strain localization, primarily attributed to the presence of Lüders banding. Notably, the average strain within the C_Mild and C_HSLA steel specimens is four times and two times

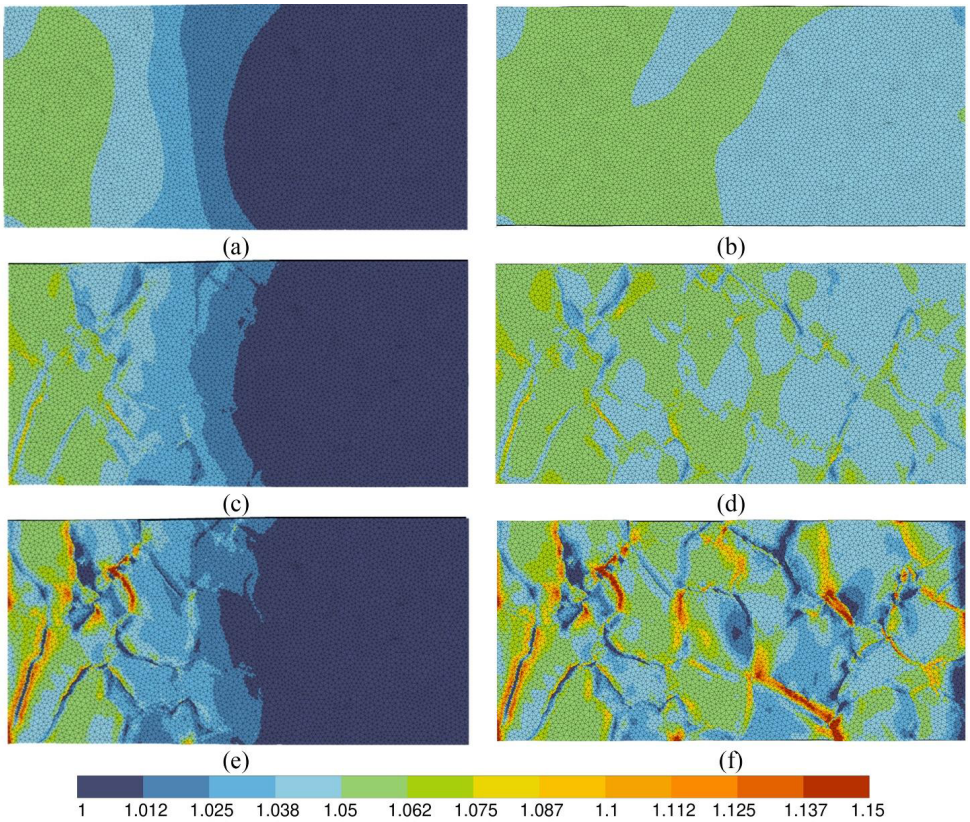

Figure 14. Distribution of the strain component F_{11} along the tensile axis for the C_HSLA steel specimen at overall strain levels 2% (left) and 4% (right): (a,b) the substrate surface (ND = 0), (c,d) at the interface and (e,f) at the coating surface (ND = 1).

greater, respectively, than that observed within the grains of the C_Dual-Phase steel specimen. Within the deformed grains, the macroscopic strain F_{11} exhibits a strain gradient, which can be attributed to the heterogeneous strain in the underlying substrate. The local strain within each grain displays heterogeneity, varying from one grain to another. Nonetheless, the average strain remains closely aligned with the local strain observed in the deformed region of the underlying substrate. In Figures 13 and 14, the progress of the Lüders band is clearly visible, separating the samples in two parts, the plastically deformed and undeformed zones. The strain field is rather smooth inside the plastic zones of the substrate. This is in contrast to the coating surface where additional strain heterogeneity is induced by the anisotropic response of the zinc grains. It is remarkable that enhanced strain levels beyond 15% are observed in some grains showing the strong impact of Lüders banding on the coating's behavior.

At the interface between the coating and the substrate, it is evident that local strain undergoes significant influence from the strain localization occurring at the zinc grain boundaries, which are notably observed at the surface (ND = 1). This influence becomes particularly pronounced when examining the distinct strain discontinuity closely linked to the precise positioning of zinc grain boundaries. This consistent observation is visually depicted in Figures 13d, 14d and 15d. Upon comparing the local strain values at the surface and those at the interface, a noticeable strain gradient emerges, signifying a reduction in strain localization compared to what is observed at the coating surface. Nevertheless, it is important to note that even at

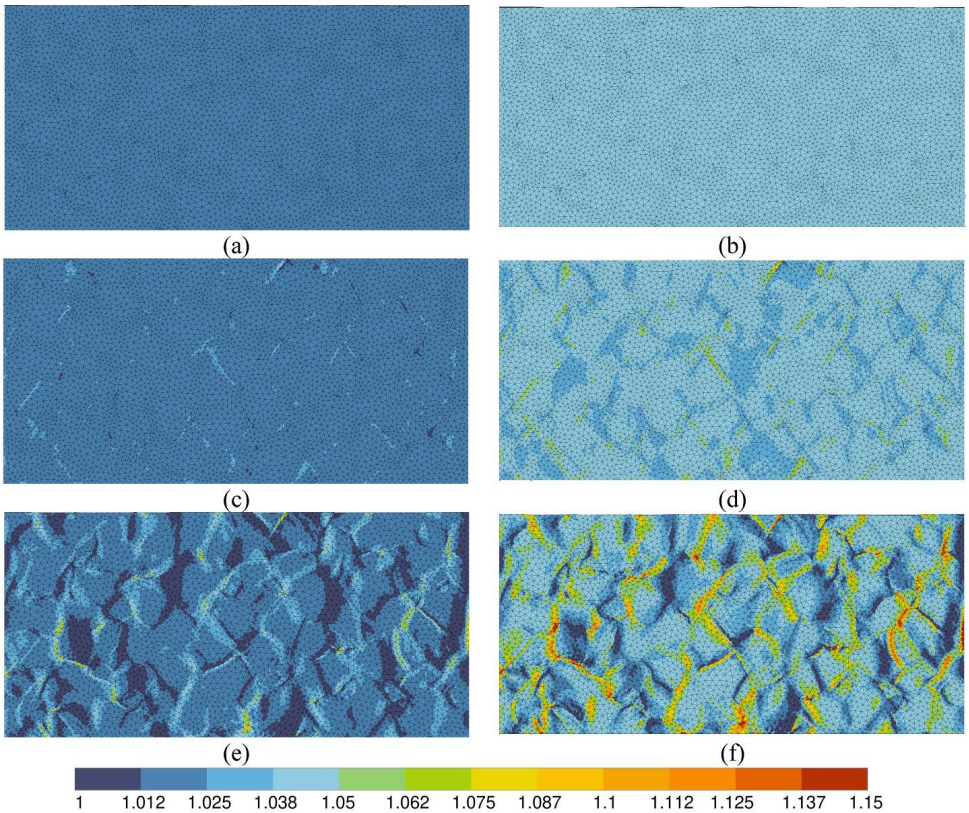

Figure 15. Distribution of the strain component F_{11} along the tensile axis for the C_Dual-Phase steel specimen at overall strain levels 2% (left) and 4% (right): (a,b) the substrate surface (ND = 0), (c,d) at the interface and (e,f) at the coating surface (ND = 1).

the interface, the intensity of strain localization remains significant in the cases of C_Mild and C_HSLA specimens, primarily due to the presence and influence of Lüders banding.

The slip activities in zinc grains are presented in Figure 16 for C_Mild, Figure 17 for C_HSLA and Figure 18 for C_Dual-Phase steel specimen. The maps show the cumulative plastic strain computed separately for each system family (it means that, for the computation of these variables, the sum is taken over all the slip systems belonging to one chosen family only).

For the C_Mild steel specimen subjected to a macroscopic strain of 4%, nearly all zinc grains exhibit deformation predominantly through basal slip as depicted in Figure 16a. Furthermore, in addition to basal sliding, some grains also undergo pyramidal slip and twinning, with a significantly lower cumulative plastic strain compared to basal slip within the same grain as presented in Figures 16b and 16c. The significant activation of basal slip at the free surface is in accordance with the experimental observations of Figure 7.

In the case of the C_HSLA steel specimen, basal slip is significantly activated, akin to the behavior observed in the C_Mild steel specimen, as illustrated in Figure 17a. Interestingly, within the deformed region, certain grains exhibit little to no basal deformation, such as grains numbered 5, 13, 14, 28, and 34. These grains are primarily characterized by c axes perpendicular to the loading direction, resulting in almost vanishing Schmid factor. Instead, Figure 17c demonstrates that these grains undergo deformation through twinning. Additionally, minor plasticity is attributed to pyramidal slip in this specimen. Similar slip activity is observed in the C_Dual-Phase

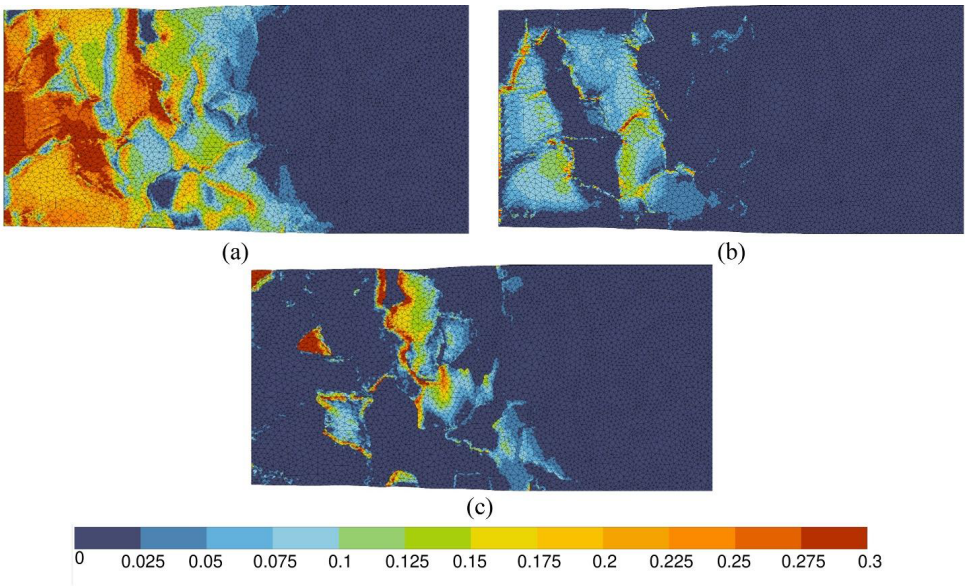

Figure 16. Slip activities at the surface of the C_Mild steel Specimen at 4% of macroscopic strain, (a) basal slip, (b) pyramidal slip and (c) twinning.

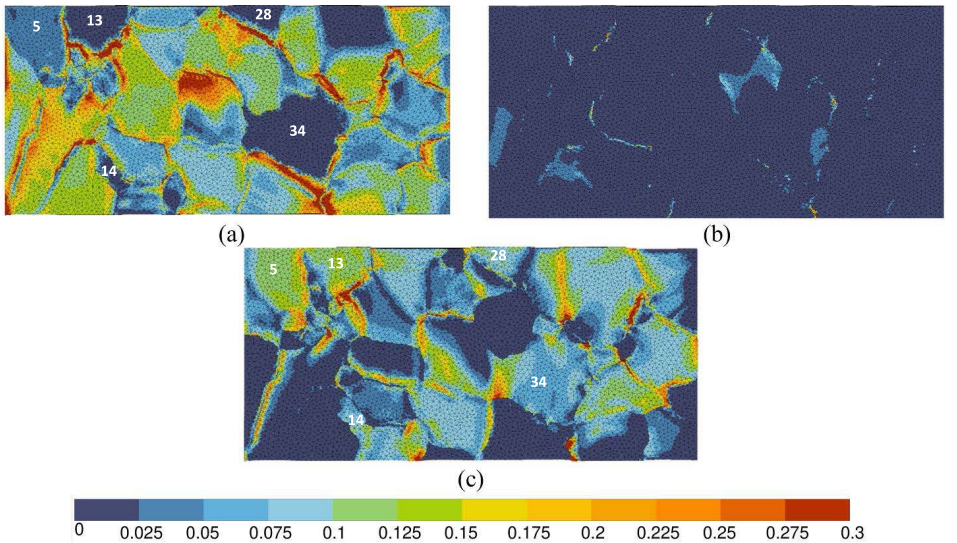

Figure 17. Slip activities at the surface of the C_HSLA steel Specimen at 4% of macroscopic strain, (a) basal slip, (b) pyramidal slip and (c) twinning.

steel specimen, with notable basal slip and twinning, and minimal activation of pyramidal slip as presented in Figure 18. Similarly, in the case of the C_HSLA steel specimen, grains within the dendritic structure that do not deform through basal slip but through twinning exhibit a c-axis orientation perpendicular to ND. Examples include grains 29, 37, 49, 64, 96, and 147. Such behavior has been experimentally observed during uniaxial testing within the deformed region as depicted in Figure 18.

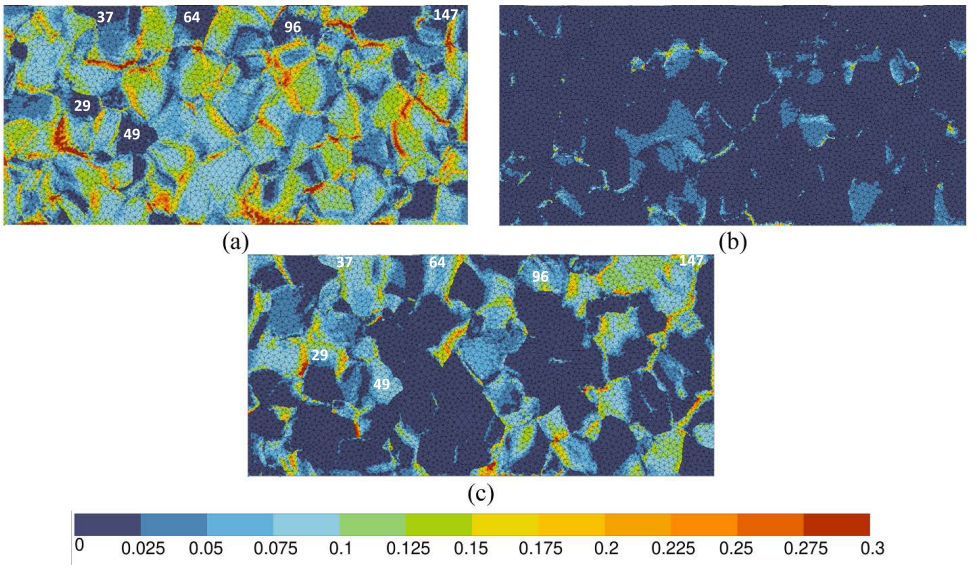

Figure 18. Slip activities at the surface of the C_Dual-Phase steel Specimen at 4% of macroscopic strain, (a) basal slip, (b) pyramidal slip and (c) twinning.

In summary, the simulation results underscore a pronounced dependence of deformation modes on the coating texture. The numerical findings corroborate that the coating primarily undergoes deformation through basal slip and twinning for grain with *c*-axis paralleled to the ND, aligning with observations from uniaxial tests. Additionally, a noticeable degree of pyramidal slip was recorded in both simulations and experimental observations. Notably, the simulations reveal that the substrate behavior in the presence of Lüders bands significantly influences the acceleration of deformation mechanisms, leading to localized deformation at the coating-substrate interface at early stages of macroscopic deformation.

5. Conclusion

In this study, a comprehensive investigation of the mechanical interaction between Zn–Al–Mg-coatings and the steel substrate, aiming to unravel the intricate mechanisms of plastic deformation and cracking. Through a meticulous blend of experimental tests, sophisticated simulations, and crystallographic analyses, the research provides invaluable insights into the complex deformation phenomena and strain localization mechanisms inherent in Zn–Al–Mg-coated steel specimens.

A primary focus of this study is the profound influence of crystallographic orientations on deformation patterns within both the coating and substrate. The incorporation of a crystal plasticity model enables a comprehensive understanding of how grain orientations dictate slip and twinning activity, leading to strong variations in plastic strain distribution. Noteworthy is the association of specific crystallographic orientations, such as (0001) parallel to the ND, with twinning.

The examination of strain distribution at various loading stages provides important insights, showcasing uniform strain fields in Dual-Phase steel and heterogeneous strain in Mild and HSLA steel specimens, attributed to the presence of Lüders banding. Particularly noteworthy is the heightened intensity of strain localization observed in the C_Mild and C_HSLA specimens, extending even beyond the interface between the coating and substrate.

Additionally, the investigation extends to the simulation of Lüders bands, shedding light on their impact on strain localization within the coating and at the coating-substrate interface. The study emphasizes the pivotal role played by the length of the Lüders plateau in different steel substrates, influencing the extent of strain localization and shaping the overall deformation behavior of the coated steel specimens.

Furthermore, the investigation into slip activities within the zinc grains revealed that basal slip is a dominant mechanism, particularly at the free surface. Twinning, as an additional deformation mechanism, was consistently observed in all three specimens, confirming experimental findings and emphasizing their significance in strain accommodation.

The knowledge obtained from this study holds significant implications for the optimization of Zn–Al–Mg coatings in industrial applications. Understanding the crystallographic aspects, strain localization, and deformation mechanisms can guide the development of predictive models to enhance the performance and longevity of these coatings.

Several simplifications in the modelling and simulation approach should be underlined. A more realistic description of the interaction of the coating grains with the substrate should include the explicit meshing of the steel microstructure, including crystal plasticity in the steel grains. This would allow for a more precise prediction of coating/substrate interface stresses and associated interface resistance. Due to the smaller steel grain size, this effect has been neglected in the present work. Twinning is an important deformation mode in zinc grains. The pseudo-slip model for twinning used in the present work does not account for the formation and propagation of fully formed twins. This limitation has been overcome in the recent paper [29] where a localized twinning model was introduced. This leads to significantly higher local stress concentration close to the interface and to strong interaction between plasticity and twinning. The work [29] also contains a detailed comparison of the experimental and simulated strain and orientation fields, based on meshing of the real microstructure. An application to the interaction of Lüders bands and twin formation and propagation is in progress. Another missing aspect is the consideration of brittle eutectic phases, which remains open in the current modelling of zinc coatings. The next steps will be dedicated to a closer identification of damage mode including cleavage [30] and spalling, not observed in the present materials in spite of high local strain values during the passage of Lüders bans. This research contributes to the broader field of advanced coatings and materials science, offering a foundation for further studies in this area.

Declaration of interests

The authors do not work for, advise, own shares in, or receive funds from any organization that could benefit from this article, and have declared no affiliations other than their research organizations.

References

[1] P. Bicao, J. Jianhua, S. Xuping, L. Zhi and Y. Fucheng, "Effects of zinc bath temperature on the coatings of hot-dip galvanizing", *Surf. Coat. Technol.* **202** (2008), no. 9, pp. 1785–1788.

[2] E. Diler, S. Rioual, B. Lescop, et al., "Chemistry of corrosion products of Zn and Mg–Zn pure phases under atmospheric conditions", *Corros. Sci.* **65** (2012), pp. 178–186.

[3] T. Prosek, N. Larché, M. Vlot, et al., "Corrosion performance of Zn–Al–Mg coatings in open and confined zones in conditions simulating automotive applications", *Mater. Corros.* **61** (2010), pp. 412–420.

[4] X. Su, J. Zhou, J. Wang, C. Wu, Y. Liu, H. Tu and H. Peng, "Thermodynamic analysis and experimental study on the oxidation of the Zn–Al–Mg coating baths", *Appl. Surf. Sci.* **396** (2017), pp. 154–160.

[5] Z. Wu, S. Sandlöbes, J. Rao, J. S. K.-L. Gibson, B. Berkels and S. Korte-Kerzel, "Local mechanical properties and plasticity mechanisms in a Zn–Al eutectic alloy", *Mater. Des.* **157** (2018), pp. 337–350.

[6] G.-M. Song and W. G. Sloof, "Characterization of the failure behavior of zinc coating on dual phase steel under tensile deformation", *Mater. Sci. Eng. A* **528** (2011), pp. 6432–6437.

[7] Z. Wu, S. Sandlöbes, J. Rao, J. S. K.-L. Gibson, B. Berkels and S. Korte-Kerzel, "Local mechanical properties and plasticity mechanisms in a Zn–Al eutectic alloy", *Mater. Des.* **157** (2018), pp. 337–350.

[8] Y. B. Park, I. G. Kim, S. G. Kim, W. T. Kim, T. C. Kim, M. S. Oh and J. S. Kim, "Orientation dependence of cracking in hot-dip Zn–Al–Mg alloy coatings on a sheet steel", *Metall. Mater. Trans. A* **48** (2017), pp. 1013–1020.

[9] G. Li and X. Long, "Mechanical behavior and damage of zinc coating for hot dip galvanized steel sheet DP600", *Coatings* **10** (2020), no. 3, article no. 202.

[10] T. Truglas, J. Duchoslav, C. Riener, M. Arndt, C. Commenda, D. Stifter, G. Angeli and H. Groiss, "Correlative characterization of Zn–Al–Mg coatings by electron microscopy and FIB tomography", *Mater. Charact.* **166** (2020), article no. 110407.

[11] M. Ahmadi, B. Salgın, B. J. Kooi and Y. Pei, "The effect of grain refinement on the deformation and cracking resistance in Zn–Al–Mg coatings", *Mater. Sci. Eng. A* **840** (2022), article no. 142995.

[12] J. He, J. Lian, A. Aretz, N. Vajragupta, U. Hangen, F. Goodwin and S. Münstermann, "Fracture properties of zinc coating layers in a galvannealed steel and an electrolytically galvanized steel", *Mater. Sci. Eng. A* **732** (2018), pp. 320–325.

[13] M. Ahmadi, B. Salgın, B. J. Kooi and Y. Pei, "Cracking behavior and formability of Zn–Al–Mg coatings: Understanding the influence of steel substrates", *Mater. Des.* **212** (2021), article no. 110215.

[14] M. Ahmadi, B. Salgın, M. Ahmadi, B. J. Kooi and Y. Pei, "Unraveling dislocation-mediated plasticity and strengthening in crack-resistant Zn–Al–Mg coatings", *Int. J. Plast.* **144** (2021), article no. 103041.

[15] R. Parisot, S. Forest, A. Pineau, F. Grillon, X. Demonet and J.-M. Mataigne, "Deformation and damage mechanisms of zinc coatings on hot-dip galvanized steel sheets: Part I", *Metall. Mater. Trans. A* **35** (2004), pp. 797–811.

[16] D. Jaffrey, J. D. Browne and T. J. Howard, "The cracking of zinc spangles on hot-dipped galvanized steel", *Metall. Trans. B* **11** (1980), pp. 631–635.

[17] R. Parisot, S. Forest, A. Pineau, F. Grillon, X. Demonet and J.-M. Mataigne, "Deformation and damage mechanisms of zinc coatings on hot-dip galvanized steel sheets: Part II", *Metall. Mater. Trans. A* **35** (2004), pp. 813–823.

[18] H. Yokoi, N. Takata, A. Suzuki and M. Kobashi, "Formation sequence of Fe–Al intermetallic phases at interface between solid Fe and liquid Zn–6Al–3Mg alloy", *Mater. Sci. Eng. A* **109** (2019), pp. 74–84.

[19] K. Honda, K. Ushioda and W. Yamada, "Influence of Si addition to the coating bath on the growth of the Al–Fe alloy layer in hot-dip Zn–Al–Mg alloy-coated steel sheets", *ISIJ Int.* **51** (2011), pp. 1895–1902.

[20] Y. Xie, A. Du, X. Zhao, R. Ma, Y. Fa and X. Cao, "Effect of Mg on Fe–Al interface structure of hot–dip galvanized Zn–Al–Mg alloy coatings", *Surf. Coat. Technol.* **337** (2018), pp. 313–320.

[21] A. Minenkov, T. Mörtlbauer, M. Arndt, G. Hesser, G. Angeli and H. Groiss, "Towards a dependable TEM characterization of hot-dip galvanized steels with low and high Si content", *Mater. Des.* **227** (2023), article no. 111684.

[22] R. Becker and S. Panchanadeeswaran, "Effects of grain interactions on deformation and local texture in polycrystals", *Acta Metall. Mater.* **43** (1995), no. 7, pp. 2701–2719.

[23] F. Bachmann, R. Hielscher and H. Schaeben, "Texture analysis with MTEX—free and open source software toolbox", in *Texture and Anisotropy of Polycrystals III*, Solid State Phenomena, vol. 160, Trans Tech Publications Ltd.: Wollerau, 2010.

[24] D. Depriester and R. Kubler, "Mtex2gmsh: a tool for generating 2D meshes from EBSD data", *J. Open Source Softw.* **5** (2020), no. 52, article no. 2094.

[25] C. Geuzaine and J.-F. Remacle, "Gmsh: a 3-D finite element mesh generator with built-in pre- and post-processing facilities", *Int. J. Numer. Methods Eng.* **79** (2009), no. 11, pp. 1309–1331.

[26] A. Marais, M. Mazière, S. Forest, A. Parrot and P. Le Delliou, "Identification of a strain-aging model accounting for Lüders behavior in a C–Mn steel", *Philos. Mag.* **92** (2012), no. 28–30, pp. 1–21.

[27] M. Mazière and S. Forest, "Strain gradient plasticity modeling and finite element simulation of Lüders band formation and propagation", *Continuum Mech. Thermodyn.* **27** (2015), pp. 83–104.

[28] K. H. Adams and T. Vreeland Jr., "Impurity effects on basal dislocation in zinc single crystals", *Trans. Metall. Soc. AIME* **242** (1968), pp. 132–139.

[29] A. Zouari, M. Bengoetxea-Aristondo, F. Siska, et al., "Experimental and digital twinning in ZnAlMg coatings", *Mech. Mater.* **199** (2024), article no. 105173.

[30] H. E. Chaieb, V. Maurel, K. Ammar, et al., "In-situ localization of damage in a Zn–Al–Mg coating deposited on steel by continuous hot-dip galvanizing", *Scr. Mater.* **243** (2024), article no. 115960.